RSC Advances

ROYAL SOCIETY OF CHEMISTRY

PAPER

View Article Online
View Journal | View Issue

Cite this: *RSC Adv.*, 2022, **12**, 26945

A Eu(III) metal–organic framework based on anthracenyl and alkynyl conjugation as a fluorescence probe for the selective monitoring of Fe^{3+} and TNP†

Yue Zhao,[ab] Chang-An Wang,[b] Ji-Kun Li,[b] Qian-Li Li,[a] Qiang Guo,[a] Jing Ru,[a] Chun-Lin Ma *[a] and Yin-Feng Han *[bc]

Received 7th May 2022
Accepted 3rd September 2022

DOI: 10.1039/d2ra02892a

rsc.li/rsc-advances

In this work, a luminescent metal–organic framework (Eu-MOF $\{[Eu_6L_6(\mu_3\text{-}OH)_8(H_2O)_3]_8 \cdot H_2O\}_n$) was constructed by a solvothermal method with a linear organic ligand L (10-[(2-amino-4-carboxyl-phenyl) ethynyl]anthracene-9-carboxylic acid) based on anthracene and alkyne groups and using Eu^{3+} as the metal center. The MOF exhibits a stable UiO-66 crystal structure, and a six-core cluster twelve-linked secondary structural unit was successfully synthesized using 2-fluorobenzoic acid as a modulator, forming a classical fcu topology. Moreover, it exhibits good chemical stability. Interestingly, Eu-MOF exhibited high selectivity and sensitive fluorescence burst properties towards Fe^{3+} ions and 2,4,6-trinitrophenol (TNP) in DMF solution. For Fe^{3+}, the K_{SV} value is 5.06×10^5 M^{-1} and the LOD value is 5.1×10^{-7} M. For TNP, the K_{SV} value is 1.92×10^4 M^{-1} and the LOD value is 1.93×10^{-6} M. In addition, Eu-MOF showed good anti-interference ability and fast response. This work provides an excellent fluorescent sensor for the detection of Fe^{3+} and 2,4,6-trinitrophenol (TNP) residues in contaminants.

1. Introduction

Environmental pollution is a serious problem in modern society.[1,2] With the development of modern industries, a great number of toxic and harmful substances are discharged into the environment.[3] These pollutants enter the human body, causing metabolic disorders and even damage to organs and tissues.[4] For example, metal ions are common inorganic contaminants due to their application in the metallurgical industry. Metal ions play an important role in biochemical processes such as biomineralization, signal transduction, metabolism, osmotic maintenance, proliferation and catalysis, and are essential elements for all life forms.[5–7] Among them, Fe^{3+} ions play an integral role due to their involvement in oxygen transport and biological processes such as in myoglobin and hemoglobin, and excess or deficiency of Fe^{3+} ions can lead to environmental pollution and physiological diseases.[8–10] Nitro aromatic explosives (NAEs) are a type of organic pollutant, which are explosive and hard to degrade.[11] As an important NAE, TNP (2,4,6-trinitrophenol) is widely used in dyes, matches, medicines, and other fields.[12,13] However, its explosiveness is a threat to the environment.[14] Traditional detection methods, such as Raman spectroscopy (RS),[15] atomic absorption spectroscopy (AAS),[16] and liquid chromatography-tandem mass spectrometry (LC-MS),[17] are time-consuming, expensive, and involve complex sample preparation, which greatly limit their application in practical work.[18] Compared with the above methods, the MOF-based luminescent sensing technology has the advantages of sensitive and simple operation.[19,20]

In recent years, luminescent metal–organic frameworks have become the subject of much attention due to their numerous tunable sites, fast response time, and high sensitivity.[21,22] Lanthanide metal–organic frameworks (Ln-MOFs) are very popular and have been widely used as luminescent sensing materials due to their special optical properties, such as narrow emission peaks, large Stokes shifts, long luminescence lifetimes, and high quantum yields.[23–25] As luminescent sensors, MOFs synthesized from organic linkers and metal ions/clusters are widely used to detect various pollutants, such as metal cations (Ni^{2+}, Hg^{2+}, Fe^{3+}),[26–28] anions (CrO_4^{2-}, $Cr_2O_7^{2-}$, MnO_4^-, CO_3^{2-}),[29–31] nitro explosives (NB, TNP)[32–34] and antibiotics (nitrofurazone, nitrofurantoin, furazolidone).[35–37] The high tunability of MOF materials makes it possible to tune the luminescence properties by introducing different metal ions or organic ligands.[38]

[a]*Institution of Functional Organic Molecules and Materials, School of Chemistry and Chemical Engineering, Liaocheng University, Liaocheng, 252059, PR China*

[b]*Department of Chemistry and Chemical Engineering, Taishan University, Tai'an, 271021, PR China. E-mail: han@tsu.edu.cn*

[c]*State Key Laboratory of Structural Chemistry, Fujian Institute of Research on the Structure of Matter, Chinese Academy of Sciences, Fuzhou, Fujian, 350002, PR China*

† Electronic supplementary information (ESI) available. CCDC 2168453. For ESI and crystallographic data in CIF or other electronic format see https://doi.org/10.1039/d2ra02892a

In the study of MOF materials, MOFs constructed from multinuclear metal clusters usually exhibit higher chemical stability and water stability and can provide more possibilities for different material applications. Moreover, the more abundant coordination modes and more complex spatial configurations of multinuclear metal clusters are beneficial for the construction of structurally novel MOFs. In order to assemble MOFs with specific ligand structures and to enhance the fluorescence detection performance of MOFs, in this work, a linear dicarboxylic acid ligand L was designed and synthesized, and anthracenyl and alkynyl functional groups were introduced. In fact, the anthracene ring, as a highly conjugated aromatic group, makes anthracene and its derivatives possess excellent optical properties. Moreover, the introduction of an alkyne not only increases the size of the organic linker but also increases the conjugation of the MOF. Thus, the ligand L is a π-electron-rich structure and can act as a fluorescent chromophore with a synergistic effect to increase the fluorescence property of the MOF. In order to obtain a stable UiO-66 topology, we added 2-fluorobenzoic acid as a modulator. 2-Fluorobenzoic acid can assist the self-assembly of the backbone during the synthetic process and ensure the formation of multinuclear metal clusters.

2. Experimental section

2.1. Materials and methods

All chemicals involved in the experiments were obtained from commercial sources and the reagents were not further processed. 10-[(2-Amino-4-carboxyl-phenyl)ethynyl]anthracene-9-carboxylic acid was synthesized based on the literature,[39,40] and the specific details are presented in the ESI† (Scheme S1 and Fig. S1†). The ^{1}H NMR spectra were documented with a Bruker AVANCE NEO spectrometer operating at 500 MHz. The single-crystal structure was analyzed using a Bruker SMART-1000 CCD diffractometer. The test conditions involved graphite monochromatic Mo Kα radiation. The CCDC reference number is 2 168 453 for Eu-MOF. Powder X-ray diffraction (PXRD) data were collected on a Bruker D8 Advance diffractometer with a Cu Kα X-ray source (operating at 40 kV and 40 mA) in the 2θ range of 5–50°. In addition, PXRD data obtained from mercury simulations and tests were used to determine the purity of the crystals. Thermogravimetric analysis (TGA) was performed on a Netzsch STA 449C apparatus under a flowing nitrogen atmosphere at a test rate of 10 °C min^{-1}. Photoluminescence spectroscopy was performed on a Hitachi F-7000 fluorescence spectrometer. Fluorescence lifetime data were acquired on a FLS1000 spectrophotometer analyzer from Edinburgh Instruments. X-ray photoelectron spectroscopy (XPS) was carried out using a Thermo Fisher Scientific ESCALAB Xi$^+$ spectrometer with Al Kα X-rays (1486.6 eV) as the light source.

2.2. Synthesis of Eu-MOF $\{[Eu_6L_6(\mu_3\text{-}OH)_8(H_2O)_3]_8 \cdot H_2O\}_n$

A mixture of ligand L (0.0086 g, 0.0226 mmol), $Eu(NO_3)_3 \cdot 6H_2O$ (0.02 g, 0.0448 mmol), and 2-fluorobenzoic acid (0.095 g, 0.683 mmol), was dissolved in a 3 mL solution of DMA/EtOH (5 : 1, v/v) in a teflon-lined stainless steel vessel (10 mL). After ultrasonic treatment for 30 min, the sample was then heated at 105 °C for 3 days, yielding 8 mg of crystals, and the reaction product was naturally cooled to room temperature. The resulting crystals were filtered out, washed with mother liquor, and dried in air. Elemental analysis of Eu-MOF ($C_{144}H_{138}Eu_6N_6O_{43}$): found: Eu = 25.71%, C = 48.72%, H = 3.99%, N = 2.40%, O = 19.40% without considering the guest molecules.

2.3. X-ray crystallography

Single-crystal X-ray diffraction data were obtained on a Bruker SMART-1000 CCD diffractometer under the following conditions: graphite monochromatic Mo Kα ($\lambda = 0.71073$ Å) radiation at room temperature. The crystal structure was obtained in the SHELXS-18 software and refined on F^2 by full-matrix least squares in the SHELXTL-18 crystallography software package. The crystallographic data are listed in Table 1, and the bond lengths and bond angles of the crystals are shown in Table 1 and S1.†

3. Results and discussion

3.1. Structural description of Eu-MOF

According to the single-crystal X-ray diffraction analysis, Eu-MOF exhibits a 3D framework of the space group $Fm\bar{3}m$ in the cubic crystal system. Each Eu(III) center is nine-coordinated by four OH^- groups (O_{1A}, O_{1B}, O_{1C}, and O_{1D}) from different anthracene-based ligands, four oxygen atoms (O_{2A}, O_{2B}, O_{2C}, and O_{2D}) from four carboxylic groups and one water molecule,

Table 1 Crystallographic data and structure refinement parameters for Eu-MOF

Complex	1
Empirical formula	$C_{144}H_{110}Eu_6N_6O_{43}$
Formula weight	3524.13
Crystal system	Cubic
Space group	$Fm\bar{3}m$
a [Å]	30.973(4)
b [Å]	30.973(4)
c [Å]	30.973(4)
α [°]	90
β [°]	90
γ [°]	90
V [Å^3]	29 713(11)
Z	4
ρ_{calc} (g cm^{-3})	0.788
μ (mm^{-1})	1.288
$F(000)$	6952.0
Crystal size (mm)	0.2 × 0.2 × 0.1
Reflections collected	37 292
Unique reflections	1354
Goodness-of-fit on F^2	1.088
Final R indices [$I > 2\sigma(I)$]	$R_1{}^a = 0.0692$ $wR_2{}^b = 0.2113$
R Indices (all data)	$R_1 = 0.0818$ $wR_2 = 0.2235$

^{a} $R_1 = \sum||F_o| - |F_c||/\sum|F_o|$. ^{b} $wR_2 = \{\sum[w(F_o^2 - F_c^2)2]/\sum[w(F_o^2)^2]\}^{.1/2}$

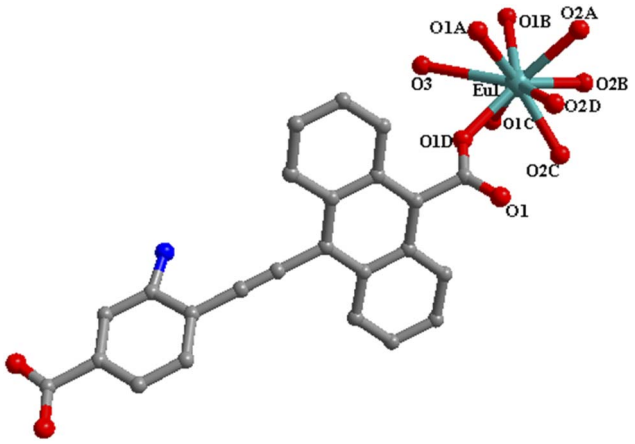

Fig. 1 A view of the asymmetric unit and some symmetry-related atoms in Eu-MOF.

while four μ-OH act as bridges to connect two metal ions (Fig. 1). The six Eu atoms are surrounded by eight μ_3-OH oxygen atoms and twelve deprotonated carboxylate oxygen atoms, forming a hexanuclear, dodeca-bonded secondary structural unit (Fig. 2a). Topologically, the secondary building units can be reduced to cuboctahedra (Fig. 2c). The disorderly linked anthracene-based ligands (Fig. 2b) can be simplified to a rod-like structure (Fig. 2d). Four secondary building blocks link 12 anthracene-based ligands to form a regular tetrahedral cage (Fig. 2e). Two regular tetrahedral cages form regular octahedral cages, and each regular octahedral cage includes 6 secondary building blocks and 24 anthracene-based ligands (Fig. 2f). The 3D structural diagram of Eu-MOF can be simplified to the topology of fcu (Fig. 2g).

3.2. PXRD pattern and stability of Eu-MOF

In order to verify the purity of the crystal, the pattern of the prepared Eu-MOF was compared with the simulated pattern of the crystal using powder X-ray diffraction (PXRD), and it was found that the patterns were in good agreement. Eu-MOF was soaked in acid-base solutions of different pH for 12 h at room temperature, and their PXRD patterns were then examined, showing good stability (Fig. S2†). The above experiments exhibit that Eu-MOF has outstanding acid-base tolerance.

3.3. Thermogravimetric analysis of Eu-MOF

The TGA profiles of Eu-MOF are presented in Fig. S3.† The whole process includes the loss of solvent molecules and the collapse of the framework. As shown in the figure, the first rapid

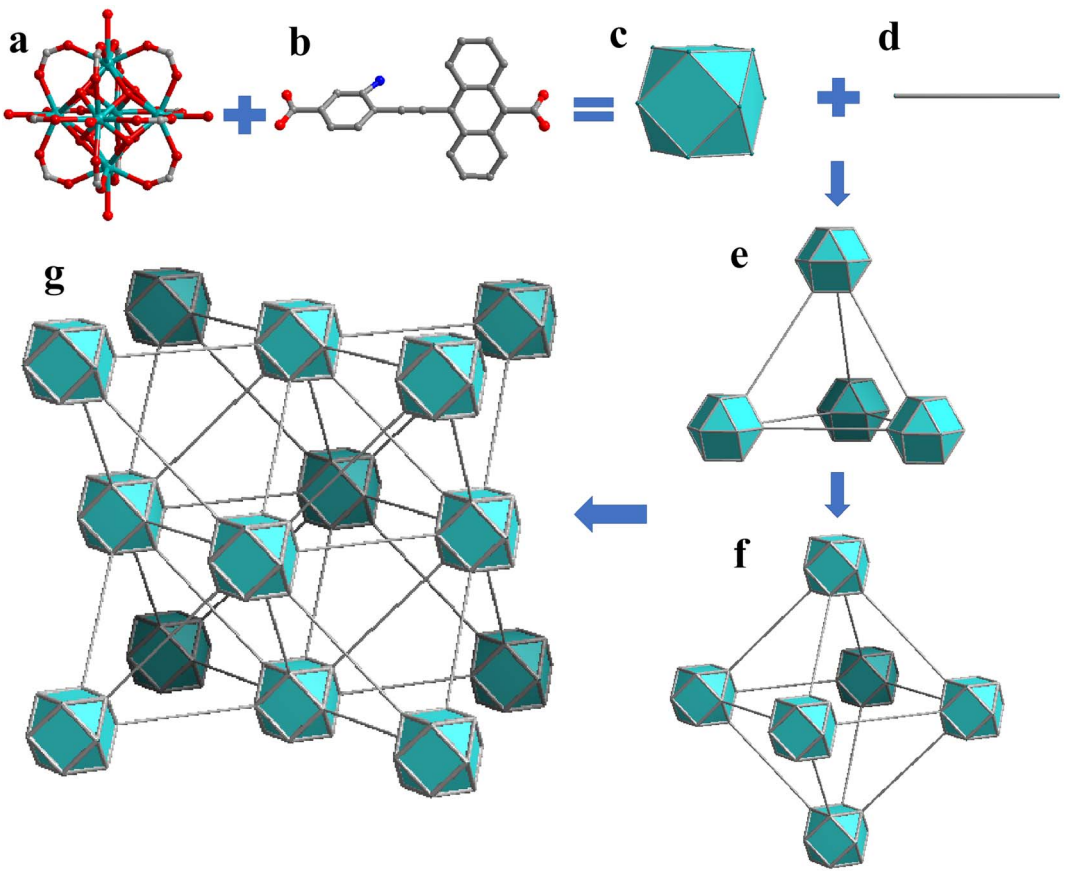

Fig. 2 (a) The secondary building unit $[Eu_6(\mu_3\text{-}OH)_8(CO_2)_{12}]$. (b) Deprotonated anthracene-based ligands. (c) Simplified structure of $[Eu_6(\mu_3\text{-}OH)_8(CO_2)_{12}]$. (d) Simplified structures of the anthracene-based ligands. (f) Simplified regular octahedral cage. (e) Simplified regular tetrahedral cage. (g) Simplified topology.

weight loss of Eu-MOF occurred in the temperature range of 70–190 °C. The weight loss here can be explained as the loss of DMA and EtOH molecules in the crystal pores. The evaporation of solvent molecules attached to the metal sites caused a second weight loss. This event occurred in the temperature range of 190–400 °C. From 400 °C, the frame of the crystal gradually collapsed (Fig. S3†).

3.4. Solid-state photoluminescence of Eu-MOF

As shown in Fig. S4,† at room temperature, the anthracene-based ligands showed an emission peak at 549 nm, and Eu-MOF showed an emission peak at 536 nm. From this, it is speculated that the emission of Eu-MOF should be attributed to the conjugation present in the anthracene-based ligands.

3.5. Fluorescence sensing activities for metal ions and explosives

We explored the sensing activities of Eu-MOF in different solvents. 2 mg of the Eu-MOF sample was dispersed separately into 2 mL *N*,*N*-dimethylformamide (DMF), methanol (MeOH), ethanol (EtOH), acetone, *N*,*N*-dimethylacetamide (DMA), H_2O, trichloromethane ($CHCl_3$) and acetonitrile (CH_3CN). A stable

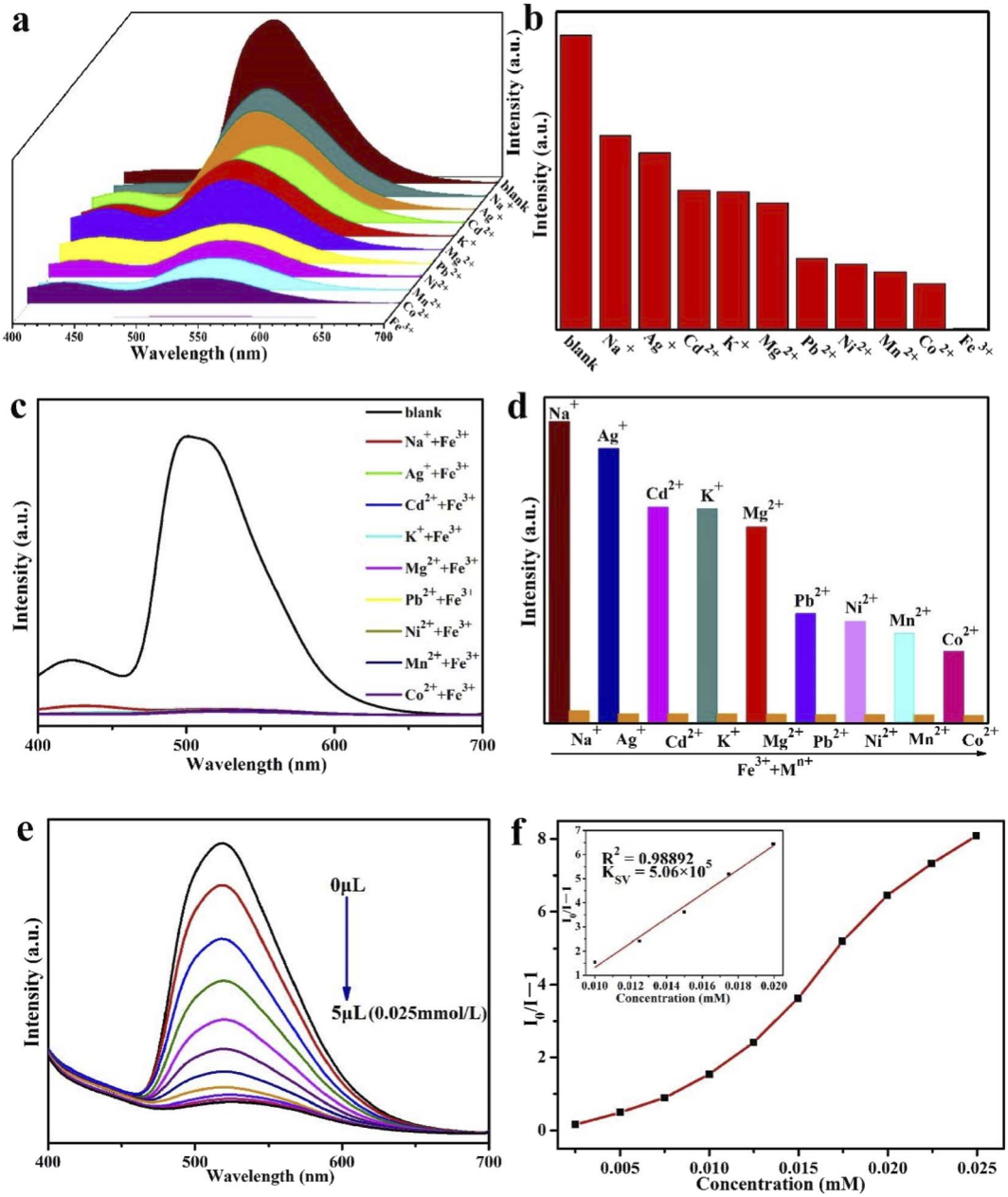

Fig. 3 (a and b) Luminescence spectra and intensities of Eu-MOF dispersed in DMF solutions with different metal ions (10^{-3} M). (c and d) Luminescence spectra of Eu-MOF with the coexistence of Fe^{3+} and other metal ions in aqueous solutions. (e) Influence on the emission spectra of Eu-MOF in DMF solutions by the addition of Fe^{3+} (10^{-2} M, 0.5 μL addition every time). (f) The Stern–Volmer plots of 0–5 μL Fe^{3+} addition; inset: linear correlation of 2–4 μL Fe^{3+}.

suspension was formed after 30 min of sonication, and the luminescence properties of these solvents were measured. As shown in Fig. S5,† Eu-MOF shows a main emission peak at 520 nm and has different emission intensities in different organic solvents. Among them, Eu-MOF was quenched in trichloromethane and acetonitrile. Notably, Eu-MOF showed the strongest fluorescence emission intensity in a DMF solution. This result indicates that the luminescence intensity of Eu-MOF has an obvious relationship with the solvent molecules. In addition, the PXRD patterns of Eu-MOF after soaking in various solvents for 30 min are almost consistent with the simulated ones, which indicates that Eu-MOF also has great stability in different solvents (Fig. S6†).

We conducted a series of tests to study the sensing properties of Eu-MOF for metal ions and explosives. 2 mg finely ground Eu-MOF was immersed in 2 mL DMF, followed by ultrasonication for 20 min to form stable suspensions. For metal cations, $M(NO_3)_x$ salts (Na^+, Ag^+, Cd^{2+}, K^+, Mg^{2+}, Pb^{2+}, Ni^{2+}, Mn^{2+}, Co^{2+}, and Fe^{3+}) with a concentration of 10^{-3} M were used. For NACs, a concentration of 10^{-4} M was used for nitrobenzene (NB), 1,3-dinitrobenzene (1,3-DNB), 3-nitrotoluene (3-NT), 4-nitrotoluene (4-NT), 2,6-dinitrotoluene (2,6-DNT), and 2,4,6-trinitrophenol

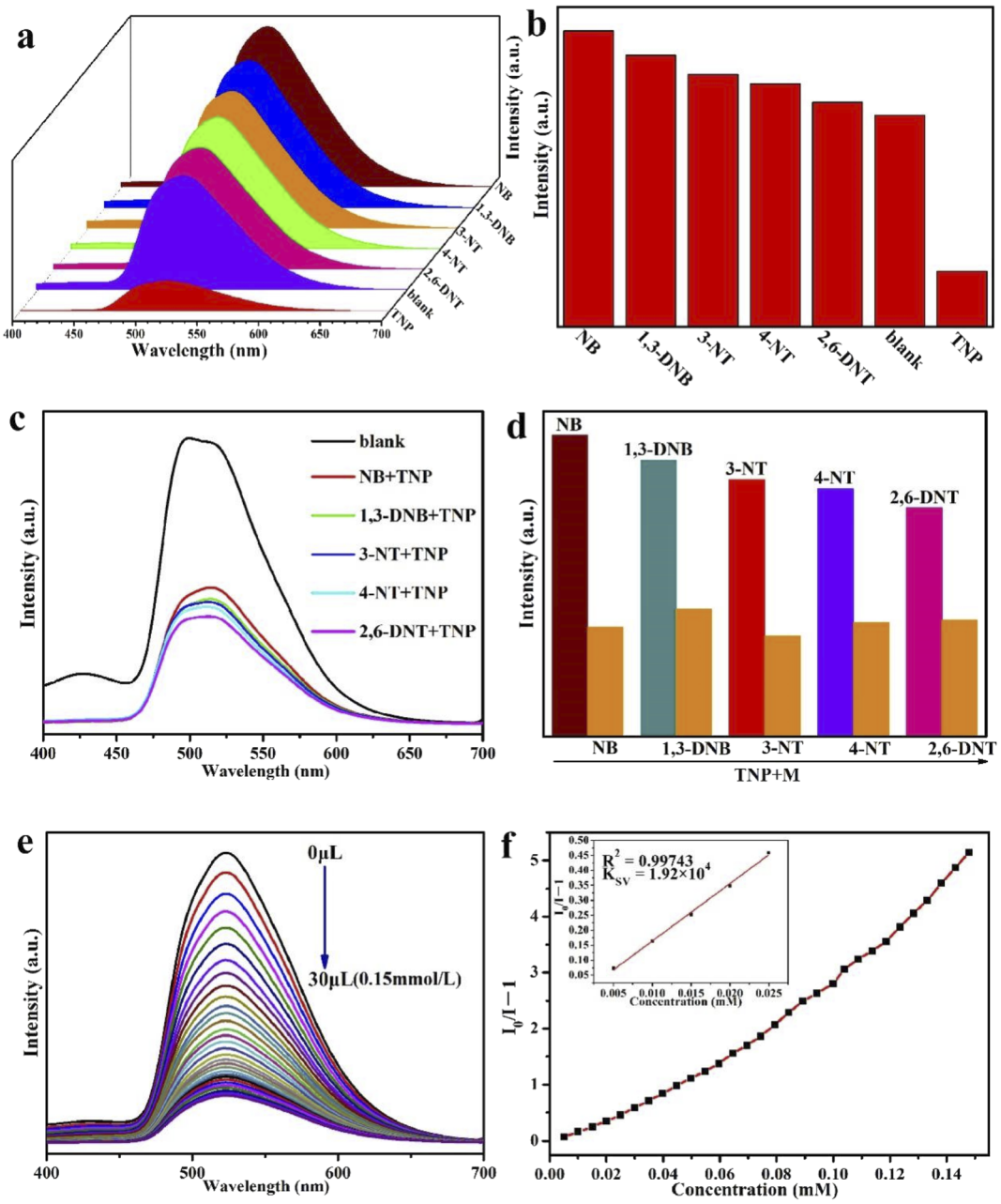

Fig. 4 (a and b) Luminescence spectra and intensities of Eu-MOF dispersed in DMF solutions with different NACs (10^{-4} M). (c and d) Luminescence spectra of Eu-MOF with the coexistence of NACs and other metal ions in aqueous solutions. (e) Influence on the emission spectra of Eu-MOF in DMF solutions by addition of TNP (10^{-2} M, 1 μL addition every time) (f) The Stern–Volmer plots of 0–30 μL TNP addition; inset: linear correlation of 0–5 μL TNP.

(TNP). In order to further to investigate the detailed performance of Eu-MOF for detecting Fe^{3+} and TNP, titration experiments were executed. The quenching constant can be fitted and calculated using the Stern–Volmer (SV) equation: $I_0/I = 1 + K_{SV}[M]$.[41] The initial intensity is I_0, the intensity after adding a certain concentration of analyte is I, and the concentration of the analyte is M. The equation $L = 3Sb/K$ is applied to calculate the limits of detection (LOD).[42] Sb is the standard deviation of the blank sample and K is the slope of the fluorescence intensity *vs.* the concentration of the test substance.

3.5.1 Metal cation detection. As shown in Fig. 4, it can be clearly observed that metal cations all cause the luminescence quenching of Eu-MOF to different degrees, while Fe^{3+} shows a remarkable effect of quenching: up to 99.5% (Fig. 3a and b). When Fe^{3+} was added, the fluorescence quenching effect is obvious in only a few seconds, indicating its excellent sensitivity towards Fe^{3+} (Fig. S7a†). Furthermore, it was observed through a series of interference tests that the quenching efficiency of Fe^{3+} by Eu-MOF was not affected when other interfering ions were present, indicating the high selectivity of Eu-MOF for Fe^{3+} (Fig. 3c and d). In addition, luminescence titration experiments showed that the fluorescence intensity of Eu-MOF decreased with a gradual increase in Fe^{3+} concentration (Fig. 3e). The LOD and K_{SV} of Fe^{3+} reached 5.1×10^{-7} M and 5.06×10^{5} M^{-1}, respectively (Fig. 3f). The high K_{SV} values and low detection limits indicate that Eu-MOF has high sensitivity and selectivity. We compared it with reported MOF materials and found that Eu-MOF has outstanding detection ability (Table S2†).

3.5.2 Nitro aromatic compound (NAC) detection. As shown in Fig. 2, after the addition of NB, 1,3-DNB, 3-NT, 4-NT and 2,6-DNT, the fluorescence intensity of Eu-MOF was significantly enhanced, but the addition of TNP produced a fluorescence quenching effect (Fig. 4a and b). The enhanced fluorescence intensity can generally be attributed to the size, conformation and chemical characteristics of the contained guest.[43] For nitro-explosives, the fluorescence enhancement may be due to the size exclusivity provided by the MOF pore structure. When certain nitro-explosive molecules enter the Eu-MOF cavity, the pore channels are occupied, which in turn affects the motion of the dye molecules, leading to a reduction in their nonradiative decay. However, the decay associated with the exciters increases, leading to the appearance of enhanced fluorescence. This could explain the fluorescence recognition phenomenon seen in Fig. 4a and b for different explosives. After adding TNP, the effect of fluorescence quenching is very obvious, and the quenching process only takes a few seconds. This phenomenon indicates that Eu-MOF is highly sensitive to TNP (Fig. S7b†). The interference test experiments show that TNP has an excellent quenching effect even in the presence of other NACs (Fig. 4c and d). Furthermore, luminescence titration experiments showed that the fluorescence intensity of Eu-MOF decreased with a gradual increase in TNP concentration. When the concentration of TNP increased to 1.5×10^{-4} M, the quenching rate was as high as 83.7% (Fig. 4e). The LOD and K_{SV} of TNP reached 1.93×10^{-6} M and 1.92×10^{4} M^{-1} (Fig. 4f), respectively. The high K_{SV} values and low detection limits indicate the high sensitivity and selectivity of Eu-MOF. The detection capability of Eu-MOF is comparable to that of other reported MOF materials (Table S3†).

3.6. Sensing mechanisms of Eu-MOF towards Fe^{3+} and TNP

The possible sensing mechanisms of Eu-MOF for Fe^{3+} and TNP were further studied. Firstly, PXRD showed that the sample could still maintain its original skeleton after the detection of Fe^{3+} and TNP, which eliminated the possibility of fluorescence quenching due to frame collapse (Fig. S8†).[44]

It is well known that fluorescence bursts will occur when the UV-vis absorption spectrum of the analyte overlaps with the excitation spectrum of the fluorescent substance,[45] which is known as the inner filter effect (IFE).[46] As shown in Fig. 5, the UV-vis absorption spectra of Fe^{3+} and TNP exhibit varying degrees of overlap with the excitation spectrum of Eu-MOF. In DMF solution, the absorption spectrum of Fe^{3+} overlaps with the excitation spectrum of Eu-MOF in the range of 375–500 nm (Fig. 5a). Similarly, in DMF solution, the absorption spectrum of TNP and the excitation spectrum of Eu-MOF also overlapped in the 410 to 500 nm range (Fig. 5b). These experiments suggest that the excitation energy of Eu-MOF has the potential to be

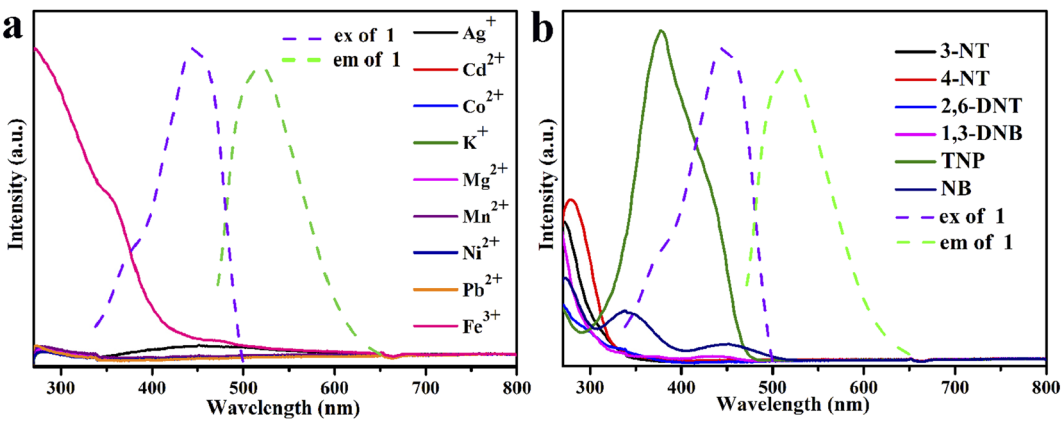

Fig. 5 Overlap between the emission (λex = 445 nm) and excitation (λem = 536 nm) spectra of Eu-MOF and the absorption spectra of metal ions (a) and NACs (b) in DMF.

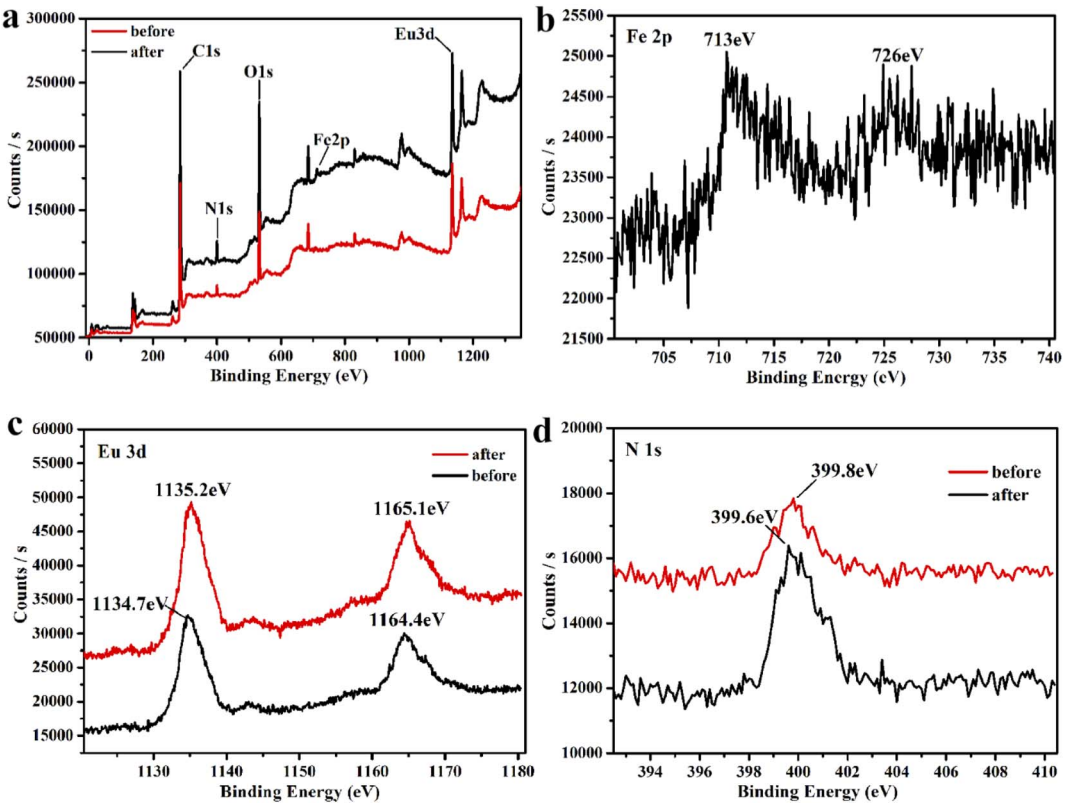

Fig. 6 (a) XPS spectra of Eu-MOF before and after immersing in Fe^{3+}. (b) The XPS shows typical peaks of Fe^{2+} at 713 and 726 eV after sensing Fe^{3+}. (c) Eu 3d XPS for Eu-MOF before and after sensing Fe^{3+}. (d) N 1s XPS for Eu-MOF before and after sensing Fe^{3+}.

absorbed by Fe^{3+} and TNP. Therefore, IFE is one of the reasons that Fe^{3+} and TNP quench the fluorescence of Eu-MOF.

Since the amino group of ligand L is uncoordinated, we speculate that there is a weak interaction between Fe^{3+} and the amino group, which leads to fluorescence burst and energy migration. Therefore, we performed X-ray photoelectron spectroscopy tests. As can be seen from Fig. S11 and S12,† the peaks of carbon and oxygen remain intact when Fe^{3+} is added to Eu-MOF, and Fig. 6b shows the characteristic peaks of Fe 2p at 713 and 726 eV. The peak of N 1s in the free amino group (Fig. 6d) is moved from the original 399.8 eV to 399.6 eV. This result indicates a weak interaction between Fe^{3+} and the amino group. Therefore, energy competition and weak interaction within the framework may have a synergistic effect on the fluorescence burst of Fe^{3+}.

In addition, the electron transfer process of the electron-rich Eu-MOF to electron-deficient NAEs is another reason for fluorescence quenching. When the analyte has a lower LUMO energy level, it is easier to receive electrons from the LUMO energy level of the fluorescent substance,[47] resulting in fluorescence quenching. As shown in Fig. S9 and Table S4,† TNP has a lower LUMO energy level than the other five NAEs,[48,49] which is accountable for its strongest quenching ability.[50,51] Meanwhile, the luminescence lifetimes of Eu-MOF in the absence or presence of TNP are nearly the same, which demonstrated that static quenching occurred in the process (Fig. S10†). Therefore, energy competition and electron transfer may have a synergistic effect on the fluorescence burst of TNP.

4. Conclusions

In conclusion, we successfully synthesized a novel three-dimensional metal–organic framework (Eu-MOF) using linear organic ligands based on anthracenyl and alkynyl groups under solvothermal conditions. Eu-MOF not only has good stability but also shows high sensitivity to the burst of Fe^{3+} and TNP. The burst constants of Eu-MOF are 5.06×10^5 M^{-1} and 1.92×10^4 M^{-1} for Fe^{3+} and TNP, respectively, and the corresponding detection limits are 5.1×10^{-7} M and 1.93×10^{-6} M. The high burst constants and low detection limits make it superior to most other reported MOF materials. In addition, we analyzed the fluorescence burst mechanism of Eu-MOF. For Fe^{3+}, the fluorescence burst may be attributed to energy competition and weak interactions between the frameworks. For TNP, we analyzed that the causes of fluorescence burst could be energy competition and electron transfer. In short, this Eu-based MOF will provide a feasible way to detect hazardous chemicals related to environmental hygiene and human health.

Conflicts of interest

The authors declare no competing financial interest.

Acknowledgements

This work was supported by the National Natural Science Foundation of China (Grant 21571137) and the Natural Science

Foundation of Shandong Province (Grant ZR2021MB060, ZR2021MB092).

References

1 A. V. Raveendran, P. A. Sankeerthana, A. Jayaraj and P. Chinna Ayya Swamy, *Results Chem.*, 2022, **4**, 100297.
2 C. Lodeiro, J. L. Capelo-Martínez, H. M. Santos and E. Oliveira, *Environ. Sci. Pollut. Res.*, 2021, **28**, 18309–18313.
3 B. B. Fischer, F. Pomati and R. I. L. Eggen, *Sci. Total Environ.*, 2013, **449**, 253–259.
4 F. Wang, F. Zhang, Z. Zhao, Z. Sun, Y. Pu, Y. Wang and X. Wang, *Dalton Trans.*, 2021, **50**, 12197–12207.
5 D. Feng, T. Zhang, T. Zhong, C. Zhang, Y. Tian and G. Wang, *J. Mater. Chem. C*, 2021, **9**, 16978–16984.
6 L. Li, Y.-F. Han, Z.-B. Zheng, C.-A. Wang, K. Nie, J.-K. Li, R.-F. Zhang, J. Ru and C.-L. Ma, *J. Solid State Chem.*, 2021, **295**, 121887.
7 Y. Cui, D. Yue, Y. Huang, J. Zhang, Z. Wang, D. Yang and G. Qian, *Chem. Commun.*, 2019, **55**, 11231–11234.
8 S. K. Panda, S. Mishra and A. K. Singh, *Dalton Trans.*, 2021, **50**, 7139–7155.
9 S. Bhowal and A. Ghosh, *RSC Adv.*, 2021, **11**, 27787–27800.
10 M. Wang, F. Huang, C. Wang, Y. Hu, P. Wu, A. Hu, J. Ji and J. Wang, *Inorg. Chem. Front.*, 2021, **8**, 4998–5005.
11 S. Dey, A. Saha, P. Kumar, C. Kar, S. Chakraborty and P. K. Sukul, *J. Photochem. Photobiol., A*, 2022, **423**, 113599.
12 M. Wang, H. W. Gao, J. X. Li, F. Y. Bai, Y. H. Xing and Z. Shi, *Dalton Trans.*, 2021, **50**, 14618–14628.
13 H. Wang, C. Chen, Y. Liu, Y. Wu, Y. Yuan and Q. Zhou, *Talanta*, 2019, **198**, 242–248.
14 L. Liu, X.-L. Chen, L. Shang, M. Cai, H.-L. Cui, H. Yang and J.-J. Wang, *Dyes Pigm.*, 2022, **202**, 110253.
15 J. Moros and J. J. Laserna, *Anal. Chem.*, 2011, **83**, 6275–6285.
16 L. Bohdálková, P. Bohdálek, E. Břízová, P. Pacherová and A. A. Kuběna, *Sci. Total Environ.*, 2018, **633**, 857–874.
17 F. Zhang, H. Yao, Y. Zhao, X. Li, G. Zhang and Y. Yang, *Talanta*, 2017, **174**, 660–666.
18 G.-L. Wen, W.-P. Wu, F.-W. Wang, D.-F. Liu, X.-L. Wang, J.-W. Rong and Y.-Y. Wang, *CrystEngComm*, 2021, **23**, 6171–6179.
19 Z. Sun, Y. Li, J. Liu, Z. Zhao, F. Wang and X. Wang, *J. Inorg. Organomet. Polym. Mater.*, 2022, **32**, 2953–2960.
20 Z. Chen, Y. Sun, L. Zhang, D. Sun, F. Liu, Q. Meng, R. Wang and D. Sun, *Chem. Commun.*, 2013, **49**, 11557–11559.
21 J.-R. Zhang, H.-Y. Zhang, J.-H. Guo, Z.-H. Liu, C.-Y. Ma, X.-G. Yang, X.-Y. Lu, J.-H. Qin and L.-F. Ma, *Dalton Trans.*, 2022, **51**, 1769–1774.
22 M. Lei, F. Ge, S. Ren, X. Gao and H. Zheng, *Sep. Purif. Technol.*, 2022, **286**, 120433.
23 X. Li, S. Lu, D. Tu, W. Zheng and X. Chen, *Nanoscale*, 2020, **12**, 15021–15035.
24 H. Shi, Y. Wang, S. Lin, J. Lou and Q. Zhang, *Dalton Trans.*, 2021, **50**, 6410–6417.
25 T. Xia, W. Cao, L. Guan, J. Zhang, F. Jiang, L. Yu and Y. Wan, *Dalton Trans.*, 2022, **51**, 5426–5433.
26 Y.-J. Kong, G.-Z. Hou, Z.-N. Gong, F.-T. Zhao and L.-J. Han, *RSC Adv.*, 2022, **12**, 8435–8442.
27 B. Qin, X. Zhang and J. Zhang, *Cryst. Growth Des.*, 2020, **20**, 5120–5128.
28 L. Guan, Z. Jiang, Y. Cui, Y. Yang, D. Yang and G. Qian, *Adv. Opt. Mater.*, 2021, **9**, 2002180.
29 Z. Sun, J. Sun, L. Xi, J. Xie, X. Wang, Y. Ma and L. Li, *Cryst. Growth Des.*, 2020, **20**, 5225–5234.
30 Z. Zhan, Y. Jia, D. Li, X. Zhang and M. Hu, *Dalton Trans.*, 2019, **48**, 15255–15262.
31 G. Tan, R.-Q. Jia, W.-L. Wu, B. Li and L.-Y. Wang, *Cryst. Growth Des.*, 2022, **22**, 323–333.
32 Y. Du, H. Yang, R. Liu, C. Shao and L. Yang, *Dalton Trans.*, 2020, **49**, 13003–13016.
33 Z. Cao, L. Chen, S. Li, M. Yu, Z. Li, K. Zhou, C. Liu, F. Jiang and M. Hong, *Chem. – Asian J.*, 2019, **14**, 3597–3602.
34 D.-D. Li, J.-H. Yu and J.-Q. Xu, *J. Solid State Chem.*, 2021, **293**, 121771.
35 S. Wu, M. Zhu, Y. Zhang, M. Kosinova, V. P. Fedin and E. Gao, *Chem. – Eur. J.*, 2020, **26**, 3137–3144.
36 Z. Lei, L. Hu, Z.-H. Yu, Q.-Y. Yao, X. Chen, H. Li, R.-M. Liu, C.-P. Li and X.-D. Zhu, *Inorg. Chem. Front.*, 2021, **8**, 1290–1296.
37 Z.-S. Qin, W.-W. Dong, J. Zhao, Y.-P. Wu, Q. Zhang and D.-S. Li, *Inorg. Chem. Front.*, 2018, **5**, 120–126.
38 H.-R. Fu, X.-X. Wu, L.-F. Ma, F. Wang and J. Zhang, *ACS Appl. Mater. Interfaces*, 2018, **10**, 18012–18020.
39 D. Chen, H. Xing, C. Wang and Z. Su, *J. Mater. Chem. A*, 2016, **4**, 2657–2662.
40 Q. Xia, X. Yu, H. Zhao, S. Wang, H. Wang, Z. Guo and H. Xing, *Cryst. Growth Des.*, 2017, **17**, 4189–4195.
41 B. Yan, *Acc. Chem. Res.*, 2017, **50**, 2789–2798.
42 Y. Li, C. Jiang, X. Chen, Y. Jiang and C. Yao, *ACS Appl. Mater. Interfaces*, 2022, **14**, 8343–8352.
43 C. Wang, L. Tian, W. Zhu, S. Wang, P. Wang, Y. Liang, W. Zhang, H. Zhao and G. Li, *ACS Appl. Mater. Interfaces*, 2017, **9**, 20076–20085.
44 Y.-T. Yan, Y. Guo, L.-N. Zheng, Y.-L. Wu, W. Cai, P.-F. Tang, X.-L. Su, W.-Y. Zhang and Y.-Y. Wang, *J. Solid State Chem.*, 2022, **309**, 122988.
45 W. Chen, J. Fan, X. Wu, D. Hu, Y. Wu, Z. Feng, M. Yan, X. Gao and J. Xie, *New J. Chem.*, 2021, **45**, 5114–5120.
46 S. Xu, J.-J. Shi, B. Ding, Z.-Y. Liu, X.-G. Wang, X.-J. Zhao and E.-C. Yang, *Dalton Trans.*, 2019, **48**, 1823–1834.
47 X. Shao, J. Wang, T. B. Marder, Z. Xie, J. Liu and L. Wang, *Macromolecules*, 2021, **54**, 6718–6725.
48 S. S. Nagarkar, B. Joarder, A. K. Chaudhari, S. Mukherjee and S. K. Ghosh, *Angew. Chem., Int. Ed.*, 2013, **52**, 2881–2885.
49 X. Zhuang, X. Zhang, N. Zhang, Y. Wang, L. Zhao and Q. Yang, *Cryst. Growth Des.*, 2019, **19**, 5729–5736.
50 M. Wang, Z. Liu, X. Zhou, H. Xiao, Y. You and W. Huang, *Inorg. Chem.*, 2020, **59**, 18027–18034.
51 X. Wang, C. Liu, M. Wang, X. Zhou, Y. You and H. Xiao, *Chem. Commun.*, 2022, **58**, 4667–4670.